

Constrained curve fitting for semi-parametric models with radial basis function networks

Anna Hasenfratz¹ and Curtis T. Peterson^{1,*}

¹*Department of Physics, University of Colorado, Boulder, Colorado 80309, USA*

Common to many analysis pipelines in lattice gauge theory and the broader scientific discipline is the need to fit a semi-parametric model to data. We propose a fit method that utilizes a radial basis function network to approximate the non-parametric component of such models. The approximate parametric model is fit to data using the basin hopping global optimization algorithm. Parameter constraints are enforced through Gaussian priors. The viability of our method is tested by examining its use in a finite-size scaling analysis of the q -state Potts model and p -state clock model with $q = 2, 3$ and $p = 4, \infty$.

I. INTRODUCTION

Fitting data to a semi-parametric model is necessary in many scientific analysis pipelines. Well-known examples from lattice gauge theory and condensed matter include spectroscopy and finite-size scaling (FSS). In both cases, the model in question contains a parametric component, from which physically relevant parameters of the model are extracted, in addition to an a priori unknown non-parametric component that is typically estimated from a generic parametric ansatz.

In a standard FSS curve collapse analysis in the vicinity of a 2nd-order phase transition, the goal is to determine the critical exponents of some scaling observable O , such as a response function. Renormalization group analysis in finite volume predicts at leading order

$$O(K, N_s) \sim N_s^{\gamma_O} \mathcal{F}_O\left((K/K_c - 1)N_s^{1/\nu}\right) \quad (K \rightarrow K_c),$$

where K refers to the coupling or temperature that becomes critical at K_c , N_s is the linear size of the system¹, ν is the critical exponent of the correlation length, and γ_O denotes the scaling dimension of the operator O . The function \mathcal{F}_O is a *universal scaling function*. The functional form of the scaling function \mathcal{F}_O is often non-parametric and a priori unknown. The FSS curve collapse analysis attempts to find K_c and the critical exponents by requiring that $O(K, N_s) N_s^{-\gamma_O}$ is described by a unique function of $(K/K_c - 1)N_s^{1/\nu}$. It is common to approximate \mathcal{F}_O with some parametric function; e.g., a polynomial or ratio of polynomials.

Another example of fitting to a semi-parametric model emerges in spectroscopy. The ground state amplitude $\tilde{\mathcal{A}}_0$ and energy \tilde{E}_0 in units of the lattice spacing a are extracted from a two-point correlation function $G(\tilde{r})$ using the ansatz

$$G(\tilde{r}) = \tilde{\mathcal{A}}_0 \exp(-\tilde{E}_0 \tilde{r}) + \sum_{i=1}^{\infty} \tilde{\mathcal{A}}_i \exp(-\tilde{E}_i \tilde{r})$$

The infinite sum over the excited-state contributions to $G(\tilde{r})$ is non-parametric in the sense that its exact evaluation requires knowledge of an infinite number of excited-state amplitudes

$\tilde{\mathcal{A}}_i$ and energies \tilde{E}_i . Estimating $\tilde{\mathcal{A}}_0$ and \tilde{E}_0 requires truncating the excited-state sum, with the order of the truncation chosen such that including higher-order terms minimally impacts the estimate of $\tilde{\mathcal{A}}_0$ and \tilde{E}_0 .

Other examples of semi-parametric models in lattice field theory, condensed matter physics and the broader scientific domain are abundant. Hence, it is desirable to have on hand a class of expressive functions that can faithfully represent the non-parametric component of such models. As universal function approximators, radial basis function networks (RBFNs) may be just the right tool. For RBFNs to be practically applicable in the high-precision setting of modern lattice gauge theory calculations, one must be able to

1. assess quality of fit and model selection criteria,
2. have a method for estimating correlated statistical uncertainties directly from a single fit, and
3. accommodate the imposition of statistical constraints and domain-specific knowledge.

We address these needs using the robust framework of Bayesian statistics and efficient implementation of the basin hopping global optimization algorithm [1].

We test the efficacy of our approach on various finite-size scaling analyses of the 2, 3-state Potts model and 4, ∞ -clock model. Though we focus on FSS for demonstration purposes, we want to stress that both the method and the network architecture that we deploy are broadly applicable to a variety of problems. We emphasize that our goal in this paper is not the precise determination of critical parameters, but to demonstrate the robust applicability of our RBFN-based method. We have made our code publicly available to facilitate the deployment and modification of the method [2].

The present paper is laid out as follows. In Sec. II, we review the structure of radial basis function networks and the tools of finite-size scaling, introducing our least-squares procedure for fitting RBFNs to data at the end. We review the q -state Potts and p -state clock models in Sec. III. In Sec. IV, we investigate the use of RBFNs in curve collapse analyses of the 2- and 3-state Potts models, along with the 4- and ∞ -state clock model. We compare RBFN interpolators against standard polynomial-based interpolations in Sec. V. We wrap up in Sec. VI with conclusions and outlook. In Appendix D, we briefly explore the use of RBFNs for direct interpolation.

* curtis.peterson@colorado.edu

¹ The lattice volume $V_d = N_s^d$ is a dimensionless quantity for symmetric lattices in d dimensions.

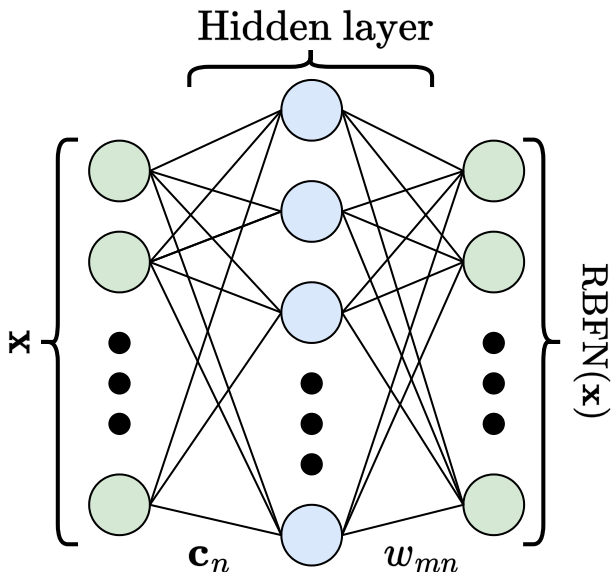


FIG. 1. Illustration of a radial basis function network (RBFN). The total number of center parameters \mathbf{c}_n , counting the components of each \mathbf{c}_n , is equal to the number of connections between the input nodes (green circles on left; a.k.a., input *features*) and hidden nodes (blue circles). The number of weights is equal to the number of connections between the hidden nodes and output nodes (green circles on right; a.k.a., output *features*).

II. FINITE SIZE SCALING WITH RADIAL BASIS FUNCTION NETWORKS

A. Radial basis function networks

Radial basis function networks (RBFNs) are artificial neural networks that possess a single hidden layer (see Fig. 1). The activation function of the hidden layer is a radial basis function (RBF) $\Phi(\cdot)$ and the output of the full network is

$$\text{RBFN}_m(\mathbf{x}) \equiv \sum_{n=1}^N w_{mn} \Phi(-\beta_n^2 \|\mathbf{x} - \mathbf{c}_n\|^2) + b_m, \quad (1)$$

where N is the number of nodes in the RBFN's hidden layer, w_{mn} are the network *weights*, b_m are the network *bias*s, β_n are the RBF *bandwidths*, and \mathbf{c}_n are the RBF *centers* [3]. We denote the parameters of the RBFN as $\Theta_{\text{RBFN}} \equiv \{w_{mn}, b_m, \beta_n, \mathbf{c}_n\}$. There are many choices for the RBFN activation. In this work, we choose the RBF to be exponential

$$\Phi(\cdot) = \exp(\cdot);$$

e.g., the activation function has a Gaussian profile. Radial basis function networks are specially designed for function approximation. According to the *universal approximation theorem* for RBFNs, the approximation accuracy of an RBFN scales with the number of nodes in its hidden layer [4]. As such, RBFNs could be a useful multitool for approximating non-parametric functions.

B. Finite size scaling with a radial basis function network

In the vicinity of a continuous phase transition at the critical value K_c of a macroscopic parameter K^2 , finite volume observables $O(K, N_s)$ scale at leading order as

$$O(K, N_s) \sim N_s^{\gamma_O} \mathcal{F}_O(x) \quad (K \rightarrow K_c), \quad (2)$$

where $x = x(K, N_s)$ is a scaling variable. The scaling function \mathcal{F}_O is an a priori unknown universal function that depends on O . The exponent γ_O is the anomalous dimension of the operator O . If the phase transition is 2nd-order,

$$x(K, N_s) = (K/K_c - 1) N_s^{1/\nu}, \quad (3)$$

where ν is the universal critical exponent of the correlation length $\xi(K)$. The same scaling is expected to hold even for first-order phase transitions, with $\nu = 1/d$ [12]. If the phase transition is ∞ -order, like the Berezinsky-Kosterlitz-Thouless (BKT) phase transition of the 2-dimensional XY model [6], the scaling variable is

$$x(K, N_s) = N_s \exp\left(-\zeta (K/K_c - 1)^{-\nu}\right), \quad (4)$$

where ζ is non-universal constant and ν is a universal critical exponent.

By simulating the system in the vicinity of K_c on multiple volumes N_s^d , it is possible to extract the critical parameters in Eqns. 2-4 by performing a simultaneous fit of $O(K, N_s)$ using several (K, N_s) values. When the critical parameters are correctly identified, the scaling function $\mathcal{F}_O(x)$ becomes independent of the volume, a phenomenon referred to as *curve collapse*. The specific form of \mathcal{F}_O is not relevant; it is non-parametric. To estimate the critical parameters from data, we parameterize \mathcal{F}_O with an RBFN and determine the parameters of the RBFN Θ_{RBFN} as part of the curve collapse.

Our RBFN-based fits to \mathcal{F}_O are performed by minimizing an augmented χ_{aug}^2 [13, 14]. We discuss our definition of χ_{aug}^2 in Appendix A. We partially control for overfitting by including in χ_{aug}^2 a term of the form

$$\chi_{\text{ridge}}^2 = \frac{1}{\lambda^2} \sum_{mn} w_{mn}^2, \quad (5)$$

which we refer to as a *ridge regression prior*, since it appeared first in the literature on ridge regression [15–18]. In the machine learning literature, adding terms of the form of Eqn. 5 to the loss is referred to as *L2-regularization* or *weight decay* [19, 20]. We also add logarithmic constraints in the form of priors to χ_{aug}^2 to force positivity on the parameters $K_c, \nu, \zeta, \gamma_O$ in Eqns. 2-4. We optimize χ_{aug}^2 using the basin hopping global optimization algorithm described in Appendix B [1].

² E.g., the temperature T in an equilibrium statistical system or bare gauge coupling g_0^2 in a gauge-fermion system at zero-temperature.

Critical parameter	2-state Potts model			3-state Potts model		
	$U_{4,\text{Potts}}^{(q)}$	$\chi_{\text{Potts}}^{(q)}$	Exact	$U_{4,\text{Potts}}^{(q)}$	$\chi_{\text{Potts}}^{(q)}$	Exact
$K_{\text{Potts}}^{(q)}$	0.881363(15)	0.881363(28)	$\log(1 + \sqrt{2})$	1.00518(15)	1.005007(48)	$\log(1 + \sqrt{3})$
ν	0.9995(27)	0.9979(40)	1	0.833(34)	0.820(23)	5/6
η	—	0.2496(29)	1/4	—	0.2713(80)	4/15

TABLE I. Comparison of our RBFN-based estimates of $K_{\text{Potts}}^{(q)}$, ν and η critical parameters for $q = 2, 3$ from a curve collapse analysis of $U_{4,\text{Potts}}^{(q)}$ and $\chi_{\text{Potts}}^{(q)}$. Exact critical parameters are from Ref. [5]. Predicted critical parameters from Figs. 2-3.

Critical parameter	4-state clock model			∞ -state clock (XY) model		
	$U_{4,\text{clock}}^{(p)}$	$\chi_{\text{clock}}^{(p)}$	Exact	$U_{4,\text{clock}}^{(p)}$	$\chi_{\text{clock}}^{(p)}$	Literature/Exact
$K_{\text{clock}}^{(p)}$	0.881379(17)	0.881430(66)	$\log(1 + \sqrt{2})$	1.126(10)	1.1160(86)	1.1199...
ζ	—	—	—	1.6(1.2)	1.45(62)	1.5...
ν	0.9976(41)	1.001(11)	1	0.55(20)	0.526(92)	1/2
η	—	0.2510(39)	1/4	—	0.2513(85)	1/4

TABLE II. Comparison of our RBFN-based estimates of $K_{\text{clock}}^{(p)}$, ν , η , and ζ critical parameters for $p = 4, \infty$ from a curve collapse analysis of $U_{4,\text{clock}}^{(p)}$ and $\chi_{\text{clock}}^{(p)}$. The exact critical parameters are from Refs. [5, 6]. Values from the literature for $K_{\text{clock},c}^{(\infty)}$ and ζ are from Refs. [7–11]. Predicted critical parameters from Figs. 4-5.

Additionally, we estimate λ using the surrogate-based empirical Bayes procedure described in Appendix C. Artificial neural networks with parameters that are estimated from an augmented χ^2 are often referred to as *Bayesian artificial neural networks* [18].

We note that the use of artificial neural networks for curve collapse was also explored in Ref. [21] using a feedforward neural network. Though we do not illustrate it in this work, we find that feedforward neural networks with Gaussian error linear activation units produce good curve collapse fits. However, we find that it is difficult to perform a stable empirical Bayes analysis using feedforward neural networks with the present strategy. Nonetheless, our fit software provides support for fitting with feedforward neural networks [2]. The authors of Ref. [21] have also made their code publicly available.

III. SUMMARY OF THE INVESTIGATED MODELS

We illustrate the efficacy of our RBFN-based fit method by studying the critical properties of several 2-dimensional spin models. This section summarizes the relevant models.

A. The q -state Potts model

The q -state Potts model is a generalization of the Ising model with spin variables taking integer values $s_i \in \{1, \dots, q\}$ [5, 22, 23]. The reduced Hamiltonian is defined as

$$\mathcal{H}_{\text{Potts}}^{(q)} = -K_{\text{Potts}}^{(q)} \sum_{\langle ij \rangle} \delta(s_i, s_j),$$

where $\langle ij \rangle$ denotes a sum over sites i and nearest-neighbors j . The Kronecker delta $\delta(s_i, s_j) = 1$ when $s_i = s_j$ and $\delta(s_i, s_j) =$

0 otherwise. We consider the q -state Potts model in $d = 2$ dimensions with $q = 2, 3$. The $q = 2$ case is equivalent to the Ising model. For all $q \geq 2$, the q -state Potts model exhibits a phase transition at³ [23]

$$K_{\text{Potts},c}^{(q)} = 1 / \log(1 + \sqrt{q}), \quad (6)$$

where the correlation length ξ in units of the lattice spacing diverges as

$$\xi(K_{\text{Potts}}^{(q)}) \propto \left| K_{\text{Potts}}^{(q)} / K_{\text{Potts},c}^{(q)} - 1 \right|^{-\nu}. \quad (7)$$

The order parameter that distinguishes the phases is the magnetization

$$M(K_{\text{Potts}}^{(q)}, N_s) \equiv \frac{1}{N_s^2} \sum_i \delta(s_i, 1) - 1/q. \quad (8)$$

The phase transition is 2nd-order for $q \leq 4$ and 1st-order for $q > 4$ [24, 25]. We list the critical exponents ν, η^4 and the critical couplings $K_{\text{Potts}}^{(q)}$ for the 2- and 3-state systems in Table I. We simulate the $q = 2, 3$ system around $K_{\text{Potts},c}^{(q)}$ using the Wolff cluster algorithm provided by the Julia-based SpinMonteCarlo library [26, 27]

B. The p -state clock model

The p -state clock model is a discrete version of the XY model. The spin variables are angles $\theta_i = 2\pi n_i/p$ for $1 \leq$

³ Note that the critical coupling for $q = 2$ differs from the conventional Ising model coupling as $K_{\text{Potts},c}^{(2)} = 2K_{\text{Ising},c}$

⁴ η is the critical exponent of the wave function, related to the critical exponent of the magnetic susceptibility as $\gamma/\nu = 2 - \eta$.

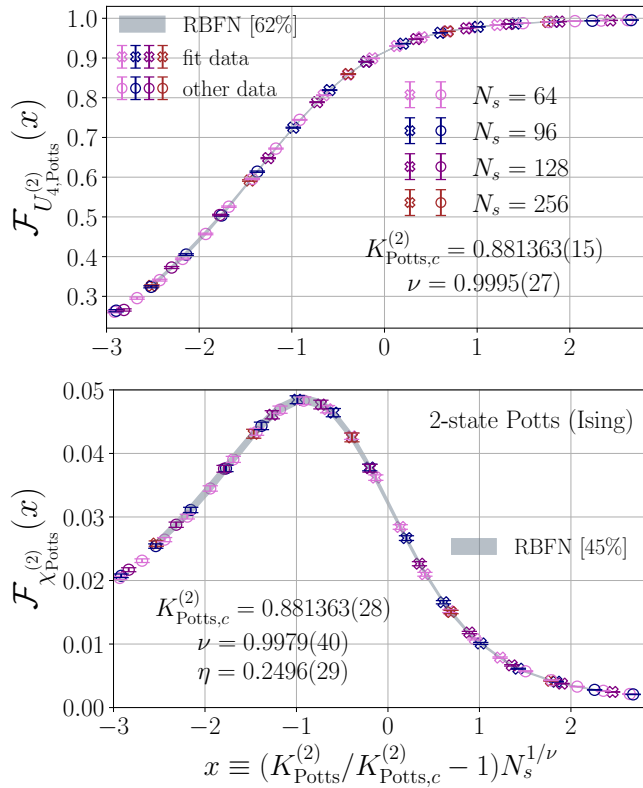


FIG. 2. RBFN-based curve collapse analysis of the 2-state Potts (Ising) model using the Binder cumulant $U_{4,\text{Potts}}^{(2)}$ (top panel) and the magnetic susceptibility $\chi_{\text{Potts}}^{(2)}$ (bottom panel). The curve collapse uses $N_s = 64$ (pink), 96 (blue), 128 (purple), and 256 (red) volumes in the coupling range $0.87 \leq K_{\text{Potts}}^{(2)} \leq 0.90$. Data used in the curve collapse are marked with an open \times (fit data); otherwise, they are marked with an open \circ (other data). The scaling function \mathcal{F}_O predicted by the RBFN is plotted as a grey band. The width of the band corresponds to the predicted error. The RBFN in the top panel has two nodes in its hidden layer and the RBFN in the bottom panel has three.

$n_i \leq p$ and the reduced Hamiltonian is defined as

$$\mathcal{H}_{\text{clock}}^{(p)} = -K_{\text{clock}}^{(p)} \sum_{\langle ij \rangle} \cos(\theta_i - \theta_j).$$

The $p = 2$ case is the Ising model and the $p \rightarrow \infty$ limit is equivalent to the XY-model. We consider the p -state clock model in $d = 2$ dimensions with $p = 4, \infty$. The 4-state clock model is in the Ising universality class [28]. It has a 2nd-order phase transition at [29]

$$K_{\text{clock}}^{(4)} = 1/\log(1 + \sqrt{2}), \quad (9)$$

where the correlation length in units of the lattice spacing diverges as Eqn. 7 with the replacement $K_{\text{Potts}}^{(q)} \rightarrow K_{\text{clock}}^{(4)}$. The ∞ -state clock (XY) model has a topology-driven ∞ -order Berezinsky-Kosterlitz-Thouless (BKT) phase transition at $K_{\text{clock},c}^{(\infty)} \approx 1.1199$ [6–11], where the correlation length in units of the lattice spacing diverges as

$$\xi(K_{\text{clock}}^{(\infty)}) \propto \exp\left(\zeta \left| K_{\text{clock}}^{(\infty)} / K_{\text{clock},c}^{(\infty)} - 1 \right|^{-\nu}\right). \quad (10)$$

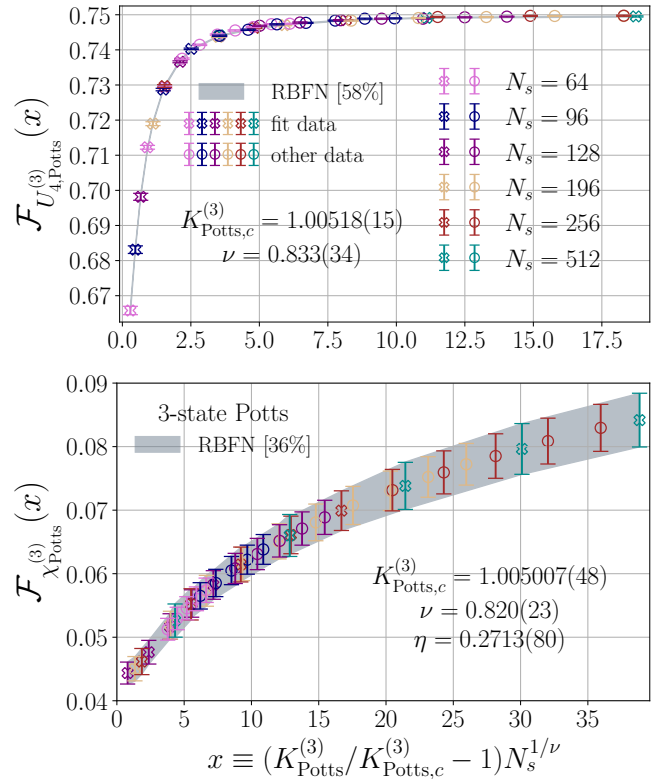


FIG. 3. RBFN-based curve collapse analysis of the 3-state Potts model using the Binder cumulant $U_{4,\text{Potts}}^{(3)}$ (top panel) and order parameter susceptibility $\chi_{\text{Potts}}^{(3)}$ (bottom panel). The curve collapse uses $N_s = 64$ (pink), 96 (blue), 128 (purple), 196 (tan), 256 (red), and 512 (cyan) volumes for $U_{4,\text{Potts}}^{(3)}$ and $N_s = 128, 196, 256,$ and 512 volumes for $\chi_{\text{Potts}}^{(3)}$ (same scheme as $U_{4,\text{Potts}}^{(3)}$). The $K_{\text{Potts}}^{(3)}$ values used in both curve collapse analyses are in the range $1.005 \leq K_{\text{Potts}}^{(3)} \leq 1.018$ for $U_{4,\text{Potts}}^{(3)}$ and $1.005 \leq K_{\text{Potts}}^{(3)} \leq 1.026$ for $\chi_{\text{Potts}}^{(3)}$. Data used in the curve collapse are marked with an open \times (fit data); otherwise, they are marked with an open \circ (other data). The scaling function \mathcal{F}_O predicted by the RBFN is plotted as a grey band. The width of the band corresponds to the predicted error. The RBFN in both panels has two nodes in its hidden layer.

The known critical parameters ζ, ν and η for the 4- and ∞ -state clock model are listed in Table II, along with the critical couplings $K_{\text{clock}}^{(p)}$. We simulate the 4-state clock model using the SpinMonteCarlo library’s implementation of the Wolff cluster algorithm. We simulate the ∞ -state clock (XY) model using Nim-based QuantumEXpressions library’s implementation of the heat bath algorithm [26, 27, 30].

IV. CURVE COLLAPSE RESULTS

A. q -state Potts model

We determine the critical parameters $K_{\text{Potts},c}^{(q)}$, ν , and η for the 2- and 3-state Potts model from a curve collapse analysis

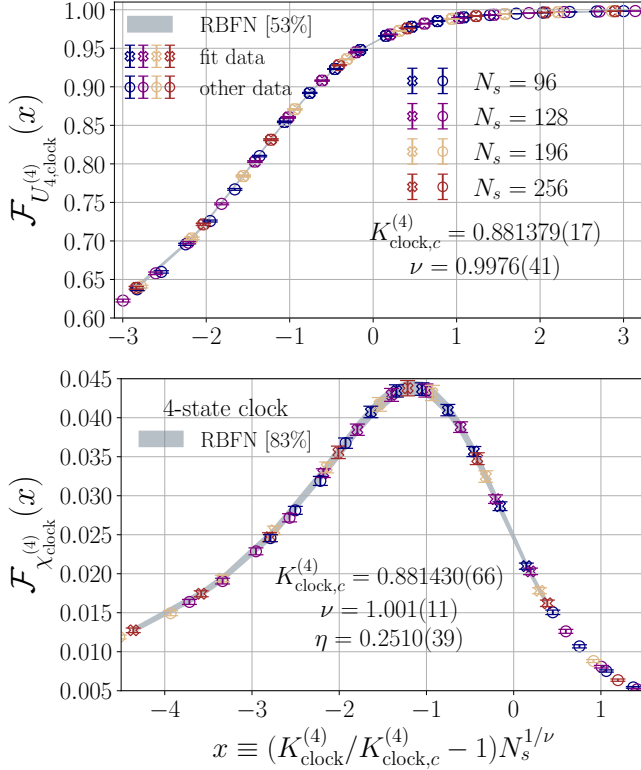


FIG. 4. RBFN-based curve collapse of the 4-state clock model using the Binder cumulant $U_{4,\text{clock}}^{(4)}$ (top panel) and connected magnetic susceptibility $\chi_{\text{clock}}^{(4)}$ (bottom panel). The curve collapse uses $N_s = 96$ (blue), 128 (purple), 196 (tan), 256 (red). The $K_{\text{clock}}^{(4)}$ values used in the curve collapse of $U_{4,\text{clock}}^{(4)}$ are in the range $0.870 \leq K_{\text{clock}}^{(4)} \leq 0.893$ and the $K_{\text{clock}}^{(4)}$ values used for $\chi_{\text{clock}}^{(4)}$ are in the range $0.870 \leq K_{\text{clock}}^{(4)} \leq 0.885$. Data used in the curve collapse is marked with an open \times (fit data); otherwise, it is marked with an open \circ (other data). The scaling function \mathcal{F}_O predicted by the RBFN is plotted as a grey band. The width of the band corresponds to the predicted error. The RBFN in both panels has three nodes in its hidden layer.

of the Binder cumulant

$$U_{4,\text{Potts}}^{(q)}(K_{\text{Potts}}^{(q)}, N_s) = \frac{1}{2} \left[3 - \frac{\langle M^4 \rangle}{\langle M^2 \rangle^2} \right] \quad (11)$$

and the connected magnetic susceptibility

$$\chi_{\text{Potts}}^{(q)}(K_{\text{Potts}}^{(q)}, N_s) = K_{\text{Potts}}^{(q)} N_s^2 \langle (|M| - \langle |M| \rangle)^2 \rangle, \quad (12)$$

where $M(K_{\text{Potts}}^{(q)}, N_s)$ is defined in Eqn. 8. In Fig. 2, we show the result of our RBFN-based curve collapse for the 2-state Potts model using the Binder cumulant (top panel) and connected magnetic susceptibility (bottom panel). We show the same information for the 3-state Potts model in Fig. 3. In Tab. I, we compare our prediction for the critical parameters $K_{\text{Potts}}^{(q)}$, ν , and $\gamma_{\chi_{\text{Potts}}^{(q)}} \equiv 2 - \eta$ with their exact values from Ref. [5]. Despite the relatively small number of nodes in each hidden layer (only 2-3), the RBFN fits the data well, with p-values

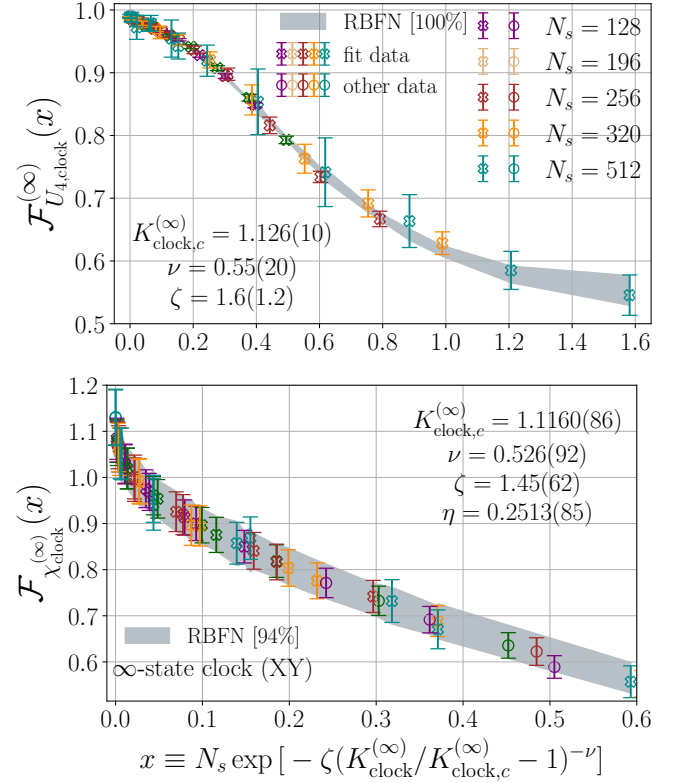


FIG. 5. RBFN-based curve collapse analysis of the ∞ -state clock (XY) model using the Binder cumulant $U_{4,\text{clock}}^{(\infty)}$ (top panel) and connected magnetic susceptibility $\chi_{\text{clock}}^{(\infty)}$ (bottom panel). The curve collapse uses $N_s = 128$ (purple), 196 (tan), 256 (red), 320 (yellow), and 512 (cyan). The $K_{\text{clock}}^{(\infty)}$ values used for both curve collapse analyses between 1.005/1.0 for $U_{4,\text{clock}}^{(\infty)}/\chi_{\text{clock}}^{(\infty)}$ and 1.1, 1.1, 1.102, 1.102, and 1.105 for $N_s = 128, 320, 256, 160$ and 512, respectively for both observables. Data used in the curve collapse is marked with an open \times (fit data); otherwise, it is marked with an open \circ (other data). The scaling function \mathcal{F}_O predicted by the RBFN is plotted as a grey band. The width of the band corresponds to the predicted error. The RBFN in both panels has two nodes in its hidden layer.

in the range 36% – 62% and predictions for the critical parameters that are in statistical agreement with their exact values from Ref. [5].

B. p -state clock model

We determine the critical parameters $K_{\text{clock},c}^{(p)}$, ν , and η for the 4- and ∞ -state clock model from a curve collapse analysis of the Binder cumulant and magnetic susceptibility. For both models, the Binder cumulant is defined similarly to Eqn. 11 using the magnitude of the magnetization vector

$$\mathbf{M}(K_{\text{clock}}^{(p)}, N_s) \equiv \sum_i (\cos(\theta_i), \sin(\theta_i)) \quad (13)$$

in place of the magnetization defined in Eqn. 8 for the Potts model. We calculate the magnetic susceptibility as in Eqn. 12

fit result	$U_{4,\text{Potts}}^{(2)}$		$\chi_{\text{Potts}}^{(2)}$		$U_{4,\text{clock}}^{(\infty)}$		$\chi_{\text{clock}}^{(\infty)}$	
	polynomial	RBFN	polynomial	RBFN	polynomial	RBFN	polynomial	RBFN
AIC/($D+k$)	1.74	0.99	1.29	1.09	1.12	0.45	0.84	0.85
$\chi_{\text{aug.}}^2/\text{d.o.f.}$	1.89	0.89	1.32	1.00	1.16	0.27	0.74	0.68
p-value	0%	62%	12%	46%	17%	100%	90%	94%
K_c	0.881335(14)	0.881363(15)	0.881420(57)	0.881363(28)	1.1568(87)	1.126(10)	1.1100(63)	1.1160(86)
ζ	—	—	—	—	2.33(24)	1.6(1.2)	0.58(19)	1.45(62)
ν	0.9954(25)	0.9995(27)	0.9913(62)	0.9979(40)	0.576(51)	0.55(20)	0.683(97)	0.526(92)
η	—	—	0.2544(54)	0.2496(29)	—	—	0.2584(56)	0.2513(85)

TABLE III. Comparison of curve collapse analysis using a polynomial (Eqn. 15) against our RBFN-based ansatz. Curve collapse analysis performed with the Binder cumulant and connected susceptibility of the 2-state Potts model and ∞ -state clock model.

using the magnitude of the magnetization defined in Eqn. 13. For the ∞ -state clock model, we obtain a better curve collapse using the estimator for the magnetic susceptibility

$$\chi_{\text{clock}}^{(\infty)}(K_{\text{clock}}^{(\infty)}, N_s) = \left\langle \left| \mathbf{M}(K_{\text{clock}}^{(\infty)}, N_s) \right|^2 \right\rangle \quad (14)$$

suggested in Refs. [31, 32]. In Tab. II, we compare our estimates for the critical parameters of both models, including ζ for the ∞ -state clock model, against both exact values and estimates from the literature.

In Figs. 4 and 5 we show the result of our curve collapse analysis of the Binder cumulant (top panels) and magnetic susceptibility (bottom panels) for the 4- and ∞ -state clock models, respectively. The p-values of our curve collapse for the 4-state clock model of both observables are 53% and 83%. For the ∞ -state clock model, they are 100% and 94%, indicating that either the RBFN overfits or the statistical errors of the data entering our curve collapse are overestimated. For both models, both exact results and values from the literature are within 1σ of our predictions. Notably, our predictions for the 4-state clock model confirm that it is not only in the Ising universality class but that it also has the same critical coupling as the 2-state Potts (Ising) model [28, 29].

V. COMPARISON AGAINST POLYNOMIAL ANSATZ

In Sec. IV, we have illustrated the robust applicability of our RBFN fit method. In this section, we contrast the RBFN with a polynomial ansatz

$$\mathcal{P}(x) = \sum_{i=0}^{P-1} p_i x^i \quad (15)$$

and ridge regression prior

$$\chi_{\text{poly. ridge}}^2 = \frac{1}{\lambda^2} \sum_{i=0}^{P-1} p_i^2. \quad (16)$$

As we do for the RBFN, we calculate λ using the surrogate-based empirical Bayes method described in Appendix C. Our comparison utilizes the $\chi_{\text{aug.}}^2/\text{d.o.f.}$ and p-value as measures of

the quality of fit, along with the Akaike information criterion (AIC) [14]

$$\text{AIC} \equiv \chi_{\text{data}}^2 + 2k, \quad (17)$$

where χ_{data}^2 is the χ^2 of the data defined in Appendix A and k is the total number of fit parameters. A good fit has $\chi_{\text{data}}^2 \approx D - k$, where D is the size of the dataset. This translates to $\text{AIC} \approx D + k$. We also compare the accuracy of predictions of critical parameters to their exact values and the literature. In all cases, the total number of parameters in Eqn. 15 is equal to the total number of parameters of the RBFN that they are being compared against.

In Table III, we compare our RBFN-based ansatz for the scaling function \mathcal{F}_O of the Binder cumulant and magnetic susceptibility for the 2-state Potts (Ising) model and ∞ -state clock (XY) model against the polynomial ansatz of Eqn. 15. The RBFN fits the 2-state Potts data the best, with a $\chi_{\text{aug.}}^2/\text{d.o.f.}$ closest to unity for both observables, along with an $\text{AIC}/(D+k)$ that is closest to unity. For the Binder cumulant in the 2-state Potts model, the polynomial ansatz predicts a value for $K_{\text{Potts},c}^{(2)}$ and ν that is greater than 1σ away from the exact value of both critical parameters. The same is true for the prediction of ν from the connected susceptibility in the 2-state Potts model. For the ∞ -state clock model, both fit ansatz overfit the data, indicating that the errors in the data are possibly overestimated. The predictions for $K_{\text{clock},c}^{(\infty)}, \zeta, \nu$ from the polynomial ansatz are greater than 1σ away from their estimates in the literature for both observables and the prediction for η from the connected susceptibility is greater than 1σ away from its exact value. All other predictions from both fit ansatz produce results that are within 1σ of either the literature or their exact values. It is clear that, with our choice of priors on the parameters of both models, the RBFN produces the most consistently correct results for the Binder cumulant and connected susceptibility of the 2-state Potts model and ∞ -state clock model.

VI. DISCUSSION AND CONCLUSION

We have investigated the use of radial basis function networks as a tool for describing the non-parametric component of semi-parameter models. For illustration, we have used an

RBFN for curve-collapse analysis of the 2, 3-state Potts model and 4, ∞ -state clock model in Sec. IV. We find that the RBFN fits a variety of disparate curves very well. Most importantly, our RBFN-based fits produce predictions for critical parameters that are consistent with their exact results and the literature. The RBFN tends to perform better than the polynomial-based fit ansatz for the scaling function with ridge regression priors given by Eqn. 16.

Though our RBFN-based fit procedure is readily available for direct use in other scientific analyses, several improvements could be made for future applications. These include improvements to the basin hopping global optimization algorithm outlined in Appendix B and a more complicated, yet efficient, empirical Bayes procedure for constraining more than just the weights of the RBFN. We have made our fit software publicly available for ease of deploying the method presented in this

work and future experimentation of both RBFNs and feedforward neural networks.

ACKNOWLEDGMENTS

Both authors acknowledge support by DOE Grant No. DE-SC0010005. This material is based upon work supported by the National Science Foundation Graduate Research Fellowship Program under Grant No. DGE 2040434. The research reported in this work made use of computing and long-term storage facilities of the USQCD Collaboration, which are funded by the Office of Science of the U.S. Department of Energy. We benefited from many comments and discussions during “The International Symposium on Lattice Field Theory” at Fermilab, Batavia, Illinois, USA, July 31 - Aug. 04, 2023.

-
- [1] David J Wales and Jonathan PK Doye, “Global optimization by basin-hopping and the lowest energy structures of lennard-jones clusters containing up to 110 atoms,” *The Journal of Physical Chemistry A* **101**, 5111–5116 (1997).
- [2] Curtis Peterson, “SwissFit,” <https://github.com/ctpeterson/SwissFit>.
- [3] Joydeep Ghosh and Arindam Nag, “An overview of radial basis function networks,” *Radial basis function networks 2: new advances in design*, 1–36 (2001).
- [4] Jooyoung Park and Irwin W Sandberg, “Universal approximation using radial-basis-function networks,” *Neural computation* **3**, 246–257 (1991).
- [5] F. Y. Wu, “The Potts model,” *Rev. Mod. Phys.* **54**, 235–268 (1982), [Erratum: *Rev. Mod. Phys.* **55**, 315–315 (1983)].
- [6] J. M. Kosterlitz, “The Critical properties of the two-dimensional XY model,” *J. Phys. C* **7**, 1046–1060 (1974).
- [7] J. M. Kosterlitz and D. J. Thouless, “Ordering, metastability and phase transitions in two-dimensional systems,” *J. Phys. C* **6**, 1181–1203 (1973).
- [8] Martin Hasenbusch, “The two-dimensional xy model at the transition temperature: a high-precision monte carlo study,” *Journal of Physics A: Mathematical and General* **38**, 5869 (2005).
- [9] Yukihiro Komura and Yutaka Okabe, “Large-scale monte carlo simulation of two-dimensional classical xy model using multiple gpus,” *Journal of the Physical Society of Japan* **81**, 113001 (2012).
- [10] Phong H Nguyen and Massimo Boninsegni, “Superfluid transition and specific heat of the 2d x-y model: Monte carlo simulation,” *Applied Sciences* **11**, 4931 (2021).
- [11] Nicholas Sale, Jeffrey Giansiracusa, and Biagio Lucini, “Quantitative analysis of phase transitions in two-dimensional XY models using persistent homology,” *Phys. Rev. E* **105**, 024121 (2022), [arXiv:2109.10960 \[cond-mat.stat-mech\]](https://arxiv.org/abs/2109.10960).
- [12] B. Nienhuis and M. Nauenberg, “First Order Phase Transitions in Renormalization Group Theory,” *Phys. Rev. Lett.* **35**, 477–479 (1975).
- [13] G. P. Lepage, B. Clark, C. T. H. Davies, K. Hornbostel, P. B. Mackenzie, C. Morningstar, and H. Trottier (HPQCD), “Constrained curve fitting,” *Nucl. Phys. B Proc. Suppl.* **106**, 12–20 (2002), [arXiv:hep-lat/0110175](https://arxiv.org/abs/hep-lat/0110175).
- [14] William I. Jay and Ethan T. Neil, “Bayesian model averaging for analysis of lattice field theory results,” *Phys. Rev. D* **103**, 114502 (2021), [arXiv:2008.01069 \[stat.ME\]](https://arxiv.org/abs/2008.01069).
- [15] David L Phillips, “A technique for the numerical solution of certain integral equations of the first kind,” *Journal of the ACM (JACM)* **9**, 84–97 (1962).
- [16] Andrei Nikolaevich Tikhonov, “On the solution of ill-posed problems and the method of regularization,” in *Doklady akademii nauk*, Vol. 151 (Russian Academy of Sciences, 1963) pp. 501–504.
- [17] Arthur E Hoerl and Robert W Kennard, “Ridge regression: Biased estimation for nonorthogonal problems,” *Technometrics* **12**, 55–67 (1970).
- [18] Kevin P Murphy, *Probabilistic machine learning: Advanced topics* (MIT press, 2023).
- [19] Theodoros Evgeniou, Massimiliano Pontil, and Tomaso Poggio, “Regularization networks and support vector machines,” *Advances in computational mathematics* **13**, 1–50 (2000).
- [20] Andriy Burkov, *The hundred-page machine learning book*, Vol. 1 (Andriy Burkov Quebec City, QC, Canada, 2019).
- [21] Ryosuke Yoneda and Kenji Harada, “Neural network approach to scaling analysis of critical phenomena,” *Phys. Rev. E* **107**, 044128 (2023), [arXiv:2209.01777 \[cond-mat.stat-mech\]](https://arxiv.org/abs/2209.01777).
- [22] R. B. Potts, “Some generalized order - disorder transformations,” *Proc. Cambridge Phil. Soc.* **48**, 106–109 (1952).
- [23] Vincent Beffara and Hugo Duminil-Copin, “The self-dual point of the two-dimensional random-cluster model is critical for $q \geq 1$,” *Probability Theory and Related Fields* **153**, 511–542 (2012).
- [24] Hugo Duminil-Copin, Maxime Gagnebin, Matan Harel, Ioan Manolescu, and Vincent Tassion, “Discontinuity of the phase transition for the planar random-cluster and potts models with $q > 4$,” *arXiv preprint arXiv:1611.09877* (2016).
- [25] Hugo Duminil-Copin, Vladas Sidoravicius, and Vincent Tassion, “Continuity of the phase transition for planar random-cluster and potts models with $1 \leq q \leq 4$,” *Communications in Mathematical Physics* **349**, 47–107 (2017).
- [26] Ulli Wolff, “Collective Monte Carlo Updating for Spin Systems,” *Phys. Rev. Lett.* **62**, 361 (1989).
- [27] Yuichi Motoyama, Morten Piibeleht, and Stefan Karpinski, “Spinmontecarlo,” <https://github.com/yomichi/SpinMonteCarlo.jl> (2019).
- [28] S. Elitzur, R. B. Pearson, and J. Shigemitsu, “The Phase Structure of Discrete Abelian Spin and Gauge Systems,” *Phys. Rev. D* **19**, 3698 (1979).

- [29] G. Ortiz, E. Cobanera, and Z. Nussinov, “Dualities and the phase diagram of the p-clock model,” *Nucl. Phys. B* **854**, 780–814 (2012), [arXiv:1108.2276 \[cond-mat.stat-mech\]](#).
- [30] J. Osborn and Xiao-Yong Jin, “Introduction to the Quantum Expressions (QEX) framework,” *PoS LATTICE2016*, 271 (2017).
- [31] Rajan Gupta and Clive F. Baillie, “Critical behavior of the two-dimensional XY model,” *Phys. Rev. B* **45**, 2883–2898 (1992).
- [32] Smita Ota, SB Ota, and M Fahnle, “Microcanonical monte carlo simulations for the two-dimensional xy model,” *Journal of Physics: Condensed Matter* **4**, 5411 (1992).
- [33] Ethan T Neil and Jacob W Sitison, “Improved information criteria for bayesian model averaging in lattice field theory,” *arXiv preprint arXiv:2208.14983* (2022).
- [34] Peter Lepage, “gvar,” (2015).
- [35] Mary Ann Branch, Thomas F Coleman, and Yuying Li, “A subspace, interior, and conjugate gradient method for large-scale bound-constrained minimization problems,” *SIAM Journal on Scientific Computing* **21**, 1–23 (1999).
- [36] Pauli Virtanen, Ralf Gommers, Travis E. Oliphant, Matt Haberland, Tyler Reddy, David Cournapeau, Evgeni Burovski, Pearu Peterson, Warren Weckesser, Jonathan Bright, Stéfan J. van der Walt, Matthew Brett, Joshua Wilson, K. Jarrod Millman, Nikolay Mayorov, Andrew R. J. Nelson, Eric Jones, Robert Kern, Eric Larson, C J Carey, İlhan Polat, Yu Feng, Eric W. Moore, Jake VanderPlas, Denis Laxalde, Josef Perktold, Robert Cimrman, Ian Henriksen, E. A. Quintero, Charles R. Harris, Anne M. Archibald, Antônio H. Ribeiro, Fabian Pedregosa, Paul van Mulbregt, and SciPy 1.0 Contributors, “SciPy 1.0: Fundamental Algorithms for Scientific Computing in Python,” *Nature Methods* **17**, 261–272 (2020).
- [37] Diederik P Kingma and Jimmy Ba, “Adam: a method for stochastic optimization (2014),” *arXiv preprint arXiv:1412.6980* **15** (2017).
- [38] Timothy Dozat, “Incorporating nesterov momentum into adam,” (2016).
- [39] Yang Xiang, Sylvain Gubian, Brian Suomela, and Julia Hoeng, “Generalized simulated annealing for global optimization: the gensa package.” *R J.* **5**, 13 (2013).
- [40] Rainer Storn and Kenneth Price, “Differential evolution—a simple and efficient heuristic for global optimization over continuous spaces,” *Journal of global optimization* **11**, 341–359 (1997).
- [41] Richard H Byrd, Peihuang Lu, Jorge Nocedal, and Ciyou Zhu, “A limited memory algorithm for bound constrained optimization,” *SIAM Journal on scientific computing* **16**, 1190–1208 (1995).
- [42] Kenneth Levenberg, “A method for the solution of certain nonlinear problems in least squares,” *Quarterly of applied mathematics* **2**, 164–168 (1944).
- [43] Donald W Marquardt, “An algorithm for least-squares estimation of nonlinear parameters,” *Journal of the society for Industrial and Applied Mathematics* **11**, 431–441 (1963).
- [44] Magnus R Hestenes, Eduard Stiefel, *et al.*, “Methods of conjugate gradients for solving linear systems,” *Journal of research of the National Bureau of Standards* **49**, 409–436 (1952).
- [45] Matthias Steffen, “A simple method for monotonic interpolation in one dimension,” *Astronomy and Astrophysics*, Vol. 239, NO. NOV (II), P. 443, 1990 **239**, 443 (1990).
- [46] Johannes E Van Himbergen and Sudip Chakravarty, “Helicity modulus and specific heat of classical xy model in two dimensions,” *Physical Review B* **23**, 359 (1981).
- [47] Luong Minh Tuan, Ta Thanh Long, Duong Xuan Nui, Pham Tuan Minh, Nguyen Duc Trung Kien, and Dao Xuan Viet, “Binder ratio in the two-dimensional q-state clock model,” *Physical Review E* **106**, 034138 (2022).

Appendix A: Augmented χ^2 and parameter estimation

In this work, we model the scaling function \mathcal{F}_O as

$$\mathcal{F}_O(K, N_s) \approx N_s^{-\gamma_O} \text{RBFN}(x(K, N_s))$$

for curve collapse (Sec. IV) or observables $O(K, N_s)$ at fixed N_s as

$$O(K, N_s) \approx \text{RBFN}(K, N_s), \quad (\text{A1})$$

for curve fitting/interpolation (Appendix D). Let us denote either model as $\mathcal{M}_\Theta(\mathbf{x})$ with model parameters Θ . When estimating the scaling function \mathcal{F}_O , Θ contains both the critical parameters and the parameters of the RBFN. When directly interpolating observables $O(K, N_s)$ at fixed N_s , Θ contains just the parameters of the RBFN. We estimate Θ by fitting \mathcal{M}_Θ to a dataset with D inputs \mathbf{x}^i and D Gaussian distributed outputs $\mathcal{D}_i \equiv \mathcal{D}(\mathbf{x}^i)$ ($1 \leq i \leq D$). Denoting the covariance of $\{\mathcal{D}_i\}_{1 \leq i \leq D}$ as Σ_D and the mean of each \mathcal{D}_i as $\bar{\mathcal{D}}_i$, we define the χ^2 of the data as

$$\chi_{\text{data}}^2(\Theta) \equiv \sum_{i,j=1}^D (\mathcal{M}_\Theta(\mathbf{x}^i) - \bar{\mathcal{D}}_i) [\Sigma_D^{-1}]_{ij} (\mathcal{M}_\Theta(\mathbf{x}^j) - \bar{\mathcal{D}}_j). \quad (\text{A2})$$

Note that χ_{data}^2 is proportional to the log *likelihood* of a multivariate Gaussian model. We represent anything that we know about Θ before fitting \mathcal{M}_Θ to $\{\mathcal{D}_i\}_{1 \leq i \leq D}$ by Gaussian priors. The priors take the form of C constraints $C^k(\Theta)$ with mean \bar{C}_k and covariance Σ_C ($1 \leq k \leq C$). We define the χ^2 of the prior as

$$\chi_{\text{prior}}^2(\Theta) \equiv \sum_{k,l=1}^C (C^k(\Theta) - \bar{C}_k) [\Sigma_C^{-1}]_{kl} (C^l(\Theta) - \bar{C}_l), \quad (\text{A3})$$

which is proportional to the log of a Gaussian *prior* distribution. According to Bayes’ theorem, the log of the *posterior* distribution that is derived from our choice of likelihood (Eqn. A2) and prior (Eqn. A3) is proportional to [13, 14, 33]

$$\chi_{\text{aug.}}^2(\Theta) \equiv \chi_{\text{data}}^2(\Theta) + \chi_{\text{prior}}^2(\Theta). \quad (\text{A4})$$

When we fit \mathcal{M}_Θ to $\{\mathcal{D}_i\}_{1 \leq i \leq D}$ with C prior constraints $C^k(\Theta)$, we are calculating a *maximum a posteriori* estimate of Θ , defined by

$$\Theta^* \equiv \text{argmin}_\Theta \chi_{\text{aug.}}^2(\Theta). \quad (\text{A5})$$

The MAP estimate Θ^* is also known as the *posterior mode*. Laplace approximation of the posterior about Θ^* yields a convenient approximation of the posterior covariance Σ_Θ :

$$\begin{aligned} [\Sigma_\Theta^{-1}]_{mn} &\approx \sum_{i,j=1}^D \frac{\partial \mathcal{M}_\Theta(\mathbf{x}_i)}{\partial \Theta_m} [\Sigma_D^{-1}]_{ij} \frac{\partial \mathcal{M}_\Theta(\mathbf{x}_j)}{\partial \Theta_n} \Bigg|_{\Theta=\Theta^*} \\ &+ \sum_{k,l=1}^C \frac{\partial C^k(\Theta)}{\partial \Theta_m} [\Sigma_C^{-1}]_{kl} \frac{\partial C^l(\Theta)}{\partial \Theta_n} \Bigg|_{\Theta=\Theta^*} \end{aligned} \quad (\text{A6})$$

Algorithm 1: The basin hopping global optimization algorithm, as implemented in Ref. [1]. The LocalOptimization step utilizes the trust region reflective local optimization algorithm [35]. We use the SciPy library’s implementation of both optimization algorithms [36].

Input: Θ_0, α, T
 $\Theta \leftarrow \text{LocalOptimization}(\Theta_0)$
 $\Theta_{\text{best}} \leftarrow \Theta$
while Θ_{best} *not converged* **do**
 $\Theta' \leftarrow \text{RandomPerturbation}(\Theta, \alpha)$
 $\Theta' \leftarrow \text{LocalOptimization}(\Theta')$
 $\Theta \leftarrow \text{MetropolisCriterion}(\Theta, \Theta', T)$
 if *new* Θ_{best} **then**
 $\Theta_{\text{best}} \leftarrow \Theta$
 end
end
Output: Θ_{best}

where $\Theta_m, \Theta_n \in \Theta$. The error in Θ that is calculated from Eqn. A6 is propagated into $\mathcal{M}_\Theta(\mathbf{x})$ using the automatic Gaussian error propagation tools provided by the GVar library [34]. Specifically, the error $\sigma_{\mathcal{M}_\Theta}^2(\mathbf{x})$ of $\mathcal{M}_\Theta(\mathbf{x})$ from the error in the parameters is given by

$$\sigma_{\mathcal{M}_\Theta}^2(\mathbf{x}) = \sum_{m,n=1}^k \frac{\partial \mathcal{M}_\Theta(\mathbf{x})}{\partial \Theta_m} [\Sigma_\Theta]_{mn} \frac{\partial \mathcal{M}_\Theta(\mathbf{x})}{\partial \Theta_n}, \quad (\text{A7})$$

where k is the total number of model parameters. Correlations between $\mathcal{M}_\Theta(\mathbf{x})$ and $\mathcal{M}_\Theta(\mathbf{y})$ for any \mathbf{x}, \mathbf{y} are calculated and kept track of in an automated manner using GVar [34].

Appendix B: Optimization with basin hopping

The landscape of $\chi_{\text{aug.}}^2(\Theta)$ in Θ is complicated. Depending on the problem, the $\chi_{\text{aug.}}^2$ landscape may possess many local optima with their own basins of attraction, along with sharp barriers that separate regions in Θ space. If one uses a local optimization algorithm to calculate the posterior mode Θ^* , it is important to be careful with the initialization Θ ; otherwise, the algorithm is bound to converge to one of many local optima. One way out is to utilize a variant of stochastic gradient descent, such as the Adam optimization algorithm or its Nesterov-accelerated counterpart [37, 38]. However, such algorithms are only efficient on large datasets. Another approach is to utilize a global optimization algorithm. In this work, we deploy the basin hopping (BH) global optimization algorithm first championed in Ref. [1]. Though we do not illustrate it in this work, we find that basin hopping vastly outperforms other common global optimization algorithms, such as generalized simulated annealing and various metaheuristic evolutionary algorithms [39, 40].

The most basic implementation of BH optimizes $\chi_{\text{aug.}}^2$ by repeatedly performing a random perturbation (“hop”) of $\Theta \rightarrow \Theta'$ with step size α that is followed by a local optimization of

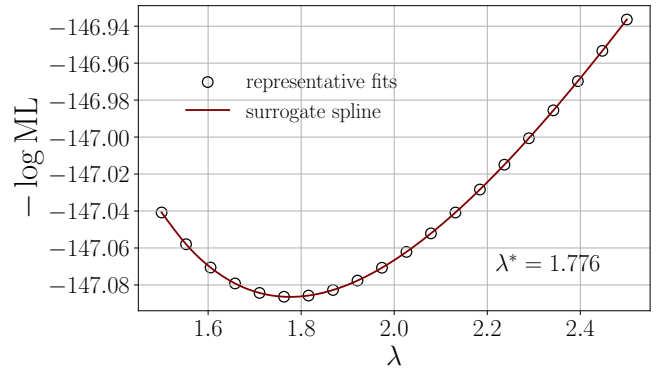


FIG. 6. Example of an interpolation over the marginal likelihood in Eqn. C1 with a cubic spline (red line). Each black circle represents the marginal likelihood calculated from a curve collapse fit of the 2-state Potts model Binder cumulant at a particular value of λ (Eqn. 5). The minimum of the surrogate spline λ^* is the value for λ suggested by the empirical Bayes procedure.

$\chi_{\text{aug.}}^2(\Theta')$ (see Algorithm 1). The optimized Θ' at each step of the algorithm is accepted with probability

$$\text{acc. prob.} = \exp \left[-\max \left(0, \chi_{\text{aug.}}^2(\Theta') - \chi_{\text{aug.}}^2(\Theta) \right) \right]^{1/T} \quad (\text{B1})$$

at the MetropolisCriterion step of Algorithm 1, where T is a hyperparameter that is referred to as the “temperature”. Our implementation of BH is built on top of the SciPy library’s implementation of BH [36].

To increase the probability of BH finding a stable global optimum, we modify the RandomPerturbation step of Algorithm 1 as follows:

1. If any parameters in Θ are restricted to the positive domain, RandomPerturbation is repeated until all positivity constraints in Θ' are satisfied.
2. Instead of utilizing a constant stepsize α , a random stepsize is drawn from $[0, \alpha]$ each time RandomPerturbation is called.

Our first modification to BH restricts the BH proposal to the appropriate domain of $\chi_{\text{aug.}}^2(\Theta)$. Our second modification empirically increases the rate at which BH finds a stable optimum.

At the LocalOptimization step of Algorithm 1, we optimize Θ' using the trust region reflective algorithm implemented in SciPy [35, 36]. Though not reported in this work, we find that the trust region reflective algorithm is very robust and outperforms many popular local optimization algorithms, such as L-BFGS-B, Levenberg-Marquardt, and conjugate gradient [41–44]. Gradients of $\chi_{\text{aug.}}^2$ with respect to Θ are calculated using the automatic differentiation tools provided by the GVar library [34].

The basin hopping algorithm is terminated after Θ_{best} in Algorithm 1 has remained the same for a pre-set number of iterations. We typically start the algorithm off with a large stepsize α , then we tune α to smaller values as $\chi_{\text{aug.}}^2(\Theta)$ decreases until

the algorithm stabilizes its sampling of $\chi_{\text{aug.}}^2(\Theta)$. We wish to explore a better procedure for automatically tuning α throughout the $\chi_{\text{aug.}}^2(\Theta)$ optimization procedure in the future. Additionally, there may be better step-taking procedures that can exploit the structure and symmetries of artificial neural networks to more efficiently explore the $\chi_{\text{aug.}}^2$ landscape.

Appendix C: Surrogate-based empirical Bayes

We calculate λ in Eqns. 5 and 16 using the empirical Bayes method discussed in Ref. [13]. Empirical Bayes picks out the value of λ that extremizes the marginal likelihood; as such, the model defined by the empirical Bayes procedure is an approximation to a full hierarchical Bayesian model [18]. We approximate the marginal likelihood using a Laplace approximation of the posterior distribution, yielding

$$-2 \log \text{ML} \approx \chi_{\text{aug.}}^2(\Theta^*) + \log \frac{(2\pi)^{\text{d.o.f.}} \det \Sigma_O \det \Sigma_C}{\det \Sigma_{\Theta^*}}. \quad (\text{C1})$$

As $\log \text{ML}$ is a function of λ , each value of $\log \text{ML}$ is calculated by performing a fit. Therefore, it is computationally advantageous to reduce the number of fits needed to be performed to optimize $\log \text{ML}$. We do so via the following three-step procedure:

1. Perform M fits in the range $[\lambda_{\text{min.}}, \lambda_{\text{max.}}]$ and estimate $\log \text{ML}$ using Eqn. C1 for each fit.
2. Interpolate over the estimate of $\log \text{ML}$ in λ for each fit using a cubic spline. We use either the monotonic or smooth spline algorithm provided by GVar [34, 45].
3. Optimize $\log \text{ML}$ by utilizing the cubic spline as a surrogate for $\log \text{ML}$.

The accuracy of λ scales with the number of fits M entering the knots of the cubic spline. Very few fits are typically needed to obtain a reasonable estimate for the $\lambda = \lambda^*$ that optimizes $\log \text{ML}$. In Fig. 6, we show an example of this procedure for our curve collapse analysis of the Binder cumulant in the 2-state Potts model discussed in Sec. IV. Each open circle represents the $\log \text{ML}$ calculated from a fit at a particular value of λ . The red line is an interpolation of $\log \text{ML}$ in λ using a cubic spline. The value $\lambda^* = 1.776$ that optimizes $\log \text{ML}$ is calculated by minimizing the value of $-\log \text{ML}$ that we estimate from the cubic spline. Though our surrogate-based empirical Bayes procedure can be implemented in an embarrassingly parallel fashion, it is numerically more stable to calculate the marginal likelihood by starting at a small value of λ , then calculate subsequent marginal likelihoods at larger λ by sequentially initializing each fit with the parameters calculated from the previous fit.

It is worth noting that this procedure could be improved by nesting it into an iterative bisection-based optimization algorithm, whereby $\lambda_{\text{min.}}, \lambda_{\text{max.}}$ converge to λ^* using the derivative of the spline-based surrogate of $\log \text{ML}$ as the number of iterations increases. The present procedure may also be extended to multiple dimensions; however, it is probably more

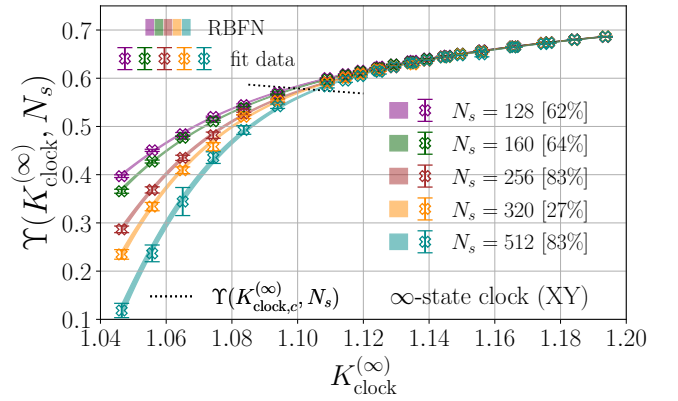


FIG. 7. RBFN-based interpolation of the helicity modulus $\Upsilon(K_{\text{clock}}^{(\infty)}, N_s)$ for the ∞ -state clock (XY) model at fixed N_s . Data included in fit is shown as an errorbar with an open “x” marker. RBFN-based interpolation is shown as a colored band. Interpolation performed on $N_s = 128$ (purple), 160 (dark green), 256 (red), 320 (yellow), and 512 (cyan). The RBFN-based fits are shown as a colored bands, with the width of the band indicating the error. The color of each band indicates the N_s at which the fit was performed. The helicity modulus at $K_{\text{clock},c}^{(\infty)}(N_s)$ given by Eqn. D4 is indicated by a dotted black line. The RBFN has 2 nodes in its hidden layer.

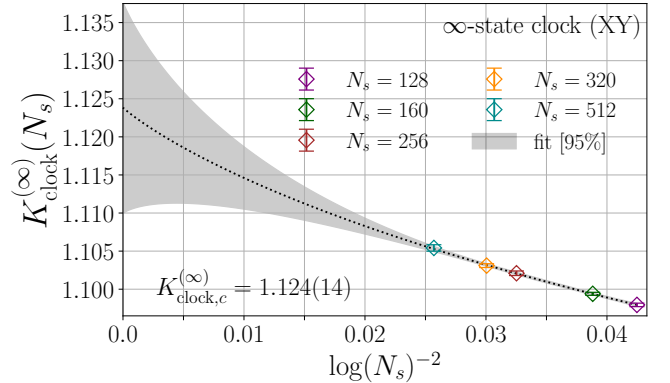


FIG. 8. Extrapolation of the pseudocritical temperature $K_{\text{clock},c}^{(\infty)}(N_s)$ calculated from the intersection of our RBFN-based interpolation (colored bands in Fig. 7) with the universal jump condition (dotted line in Fig. 7) to $1/N_s \rightarrow 0$ using Eqn. D5. The pseudocritical temperatures are indicated by multi-colored errorbars with open diamond markers “ \diamond ” and utilize the same color scheme as Fig. 7 for different N_s (see caption). Result of fit to Eqn. D5 is shown as a grey band and the central value of the fit prediction is shown as a dotted black line.

efficient to utilize a Bayesian optimization algorithm for multi-dimensional optimization of $\log \text{ML}$.

Appendix D: Interpolation

In this appendix, we demonstrate the use of RBFNs for direct interpolation. We calculate $K_{\text{clock},c}^{(\infty)}$ for the ∞ -state clock

(XY) model using the helicity modulus

$$\Upsilon(K_{\text{clock}}^{(p)}, N_s) = \frac{1}{2} \sum_{\mu=1}^2 \langle e_{\mu} - N_s^2 K_{\text{clock}}^{(p)} s_{\mu}^2 \rangle, \quad (\text{D1})$$

with

$$e_{\mu} = \frac{1}{N_s^2} \sum_{\langle ij \rangle_{\mu}} \cos(\theta_i - \theta_j), \quad (\text{D2})$$

$$s_{\mu} = \frac{1}{N_s^2} \sum_{\langle ij \rangle_{\mu}} \sin(\theta_i - \theta_j), \quad (\text{D3})$$

where $\langle ij \rangle_{\mu}$ denotes a sum of lattice sites i along the μ -direction and their nearest-neighbors j [9, 10, 46, 47]. We fit the data for $\Upsilon(K_{\text{clock}}^{(\infty)}, N_s)$ at fixed N_s with an RBFN that possess 2 nodes in its hidden layer. The fits to $\Upsilon(K_{\text{clock}}^{(\infty)}, N_s)$ yield p-values in the 27% – 83% range, as shown in Fig. 7. At $K_{\text{clock},c}^{(\infty)}$, there is a universal jump condition

$$\Upsilon(K_{\text{clock},c}^{(p)}, N_s) = 2f_r/\pi K_{\text{clock},c}^{(p)}(N_s), \quad (\text{D4})$$

where $f_r = 1 - 16\pi \exp(-4\pi)$ [10]. The universal jump condition is shown as a dotted black line in Fig. 7. By calculating where our RBFN-based interpolation of $\Upsilon(K_{\text{clock}}^{(\infty)}, N_s)$ intersects the universal jump condition, we can calculate the pseudocritical temperature $K_{\text{clock},c}^{(\infty)}(N_s)$. From $K_{\text{clock},c}^{(\infty)}(N_s)$ at multiple N_s , we extrapolate to $1/N_s \rightarrow 0$ using the ansatz

$$K_c(N_s) = K_c + \zeta^{-1/\nu} \log(\kappa N_s)^{-1/\nu}, \quad (\text{D5})$$

where κ is a free parameter and ν set to its exact value of $\nu = 1/2$ [6], as shown in Fig. 8. Our extrapolation yields a prediction for $K_{\text{clock},c}^{(\infty)}$ that is consistent with the estimates of Refs. [8–11] at the 1σ level, though with considerable statistical uncertainty due to the logarithmic scaling of $K_{\text{clock},c}^{(\infty)}(N_s)$ with N_s .